Spatially microstructured topology of chalcogenide glasses by a combination of the electrothermal process and selective etching for functional infrared media

Lara Karam, Ricardo Alvarado, Florian Calzavara, Redouane Dahmani, Myungkoo Kang, Cesar Blanco, Frédéric Adamietz, Kathleen Richardson, Marc Dussauze

Spatially-microstructured topology of chalcogenide glasses by a combination of electrothermal process and selective etching for functional infrared media

LARA KARAM,[1,*] RICARDO ALVARADO,[1] FLORIAN CALZAVARA,[1] REDOUANE DAHMANI,[1] MYUNGKOO KANG,[2] CESAR BLANCO,[2] FRÉDÉRIC ADAMIETZ,[1] KATHLEEN A. RICHARDSON,[2] AND MARC DUSSAUZE[1,**]

[1]*Institut des Sciences Moléculaires, UMR 5255 CNRS, Université de Bordeaux, 351 cours de la Libération, Talence Cedex 33405, France*
[2]*CREOL, College of Optics and Photonics, Department of Material Science and Engineering, University of Central Florida, Orlando, FL32816, USA*
**lara.karam@u-bordeaux.fr*
***marc.dussauze@u-bordeaux.fr*

Abstract: Chalcogenide glasses exhibit a wide transparency domain spanning from near infrared (IR) to mid-IR and thus, have become highly attractive optical materials in a range of applications. Controlling the topology of these glasses can be seen as a key aspect for the design of optical elements such as gratings, metasurfaces, waveguides, and other diverse refractive and diffractive optical components. Here, we demonstrate the structuring of large, millimeter square areas that have been structured at the micrometer scale employing an easy two-step process, incorporating a micro-poling step followed by immersion in an amine solvent. Ge-Sb-S-Na glasses have been investigated, and the influence of the sulphur and sodium content on the pre- and post-poling material dissolution response has been discussed. Three compositions of varying sulphur and sodium content were selected to study the influence of thermal poling using either a homogeneous or a structured electrode. It was found that either a large difference in dissolution rates of poled and unmodified regions or a large poled layer thickness leads to the generation of significant topological contrast. The origin of the poled region's selective etching has been explained on the basis of a poling-induced density decrease. Finally, it was demonstrated that when the targeted resolution is micrometric, this rather easy process could be employed as an alternative to classical lithography techniques.

1. Introduction

The control of a material's surface topology is a key aspect of its design and potential use in optical applications. In particular, a wavelength length-scale (nano- or micrometer length-scale) control is necessary to produce diffractive optical elements, [1] antireflective surfaces, [2] waveguides, [3] plasmonic surfaces [4] or metasurfaces. [5,6] Multiple processes have been shown to be suitable to structure surfaces, including lithographic techniques, which are limited to the wavelength of the tool. These methods, inherited from the microelectronic domain are among the most common and have been recently applied to low loss hybrid (diffractive/refractive) optical elements and metastructures based on chalcogenide phase change alloys. [7–9] Lithography is a cumbersome method employing multi-step processes including deposition and patterning of a photosensitive sacrificial layer, which subsequently allows the selective destruction of the material of interest's surface to realize the target structure. In each case, material-specific protocols are required, while the determination of such a 'recipe' is time consuming, and requires compatibility between resist, etchant, and writing wavelengths for each desired composition and element's design.

In the 1990's, nanoimprint lithographic techniques were developed, [10] allowing generation of low-cost, sub-25 nm structures over large areas (15 × 18 mm^2). These techniques differ from

classical lithography since a mold is employed to directly structure the desired material (generally polymeric resins). The mold, pressed against the sample (under load at temperature), generates a thickness contrast, and the compressed zones are preferentially etched or displaced for subsequent etching using either a wet or dry reactive ion etch step. Employing this technique, Kohoutek *et al.* managed to periodically structure the surface of an arsenic selenium chalcogenide glass resulting in an effective diffraction grating. [11] Here, the authors had to heat up their system to 5 °C below the glass' transition temperature (T_g) (i.e., 225 °C) in order to imprint the pattern. However, for glasses exhibiting higher T_g, the required pressure and temperature to imprint the patterns increase and can cause several problems, including higher processing costs, difficulty to realize the process over large areas, material volatilization, and reduced life expectancy of the molds. [12–14] To circumvent this difficulty, Takagi *et al.* applied an electric field and used their mold as an anode. [12] While the applied voltage in this case was only of about a hundred of volts, and the pressure was one of the driving force, the nanoimprint process employed by the authors is similar to thermal micro-poling. The thermal poling method consists of heating an amorphous material below its T_g while applying a strong electric field (several kilovolts per millimeter) with a structured electrode. [15] The sample is then brought back to room temperature before removal of the electric field. Brunkov *et al.* and Lipovskii *et al.* demonstrated a control of silicate and nano-composite glasses' surface topologies using this process. [14,16,17] However, the reliefs obtained are only (typically) tens of nanometers high which is insufficient to consider the fabrication of efficient gratings for instance. Ikutame *et al.* suggested augmenting the poling treatment with one inducing chemical attack. Here, they obtained relief heights higher with subsequent chemical attack than with poling alone. [18]

The first studies regarding chemical attacks of poled glasses date back to the early days of thermal poling. In 1974, Carlson noticed that the poled surface (hence depleted from its alkali cations) of a silicate glass was shown to be more resistant to molten alkali salts attack than the untreated surface. [19] Others relied on the difference in etching rate difference of the poled and unpoled zones to measure the poled thickness in fused silica and silicate glasses. [20,21] It is only more recently that authors started focusing on post-poling chemical attack in the optic of realizing devices such as diffraction gratings employing structured electrodes. [22] Poled silicate glasses are selectively dissolved by acidic attack, [23,24] but authors also demonstrated a dry etching route by plasma or reactive ion etching where preferential removal rates differ between poled and unpoled regions. [24,25] These two possibilities allow one to preferentially etch either the unpoled or the poled zones. It follows that the electrode's pattern can be either directly transferred on the glass' surface or negatively transferred. The step's heights obtained by these techniques on the (to-date) studied oxide glasses' family (silicate glasses) are measured to be between 0.5 and 1.2 µm.

Dissolution of chalcogenide glasses (ChGs) has been the subject of many studies since the 1980's. Numerous works focus on thin films synthesis by dissolution of bulk glasses followed by spin coating. [26–29] It was demonstrated in the last decade that sulfur glasses were effectively dissolved in amine solvents such as ethylene diamine (EDA). Furthermore, our previous works on G-Sb-S-Na glasses have shown the efficiency of micro-poling on these glassy compositions. Indeed, after the treatment, the sodium repartition, the structural modifications, the index variations, and the second harmonic optical response follow the pattern of the structured electrode. [30–32] In the present work, our aim has been to transfer the know-how realized in post-poled selective dissolution of silicate [22–24] to this chalcogenide glass system while identifying and quantifying the key parameters that can control the topologies of the resulting surfaces.

2. Experimental method

2.1 Glass synthesis

Glasses were prepared using high purity elemental Ge, Sb, and S (Alfa Aesar 99.999%). Anhydrous sodium sulfide (Na_2S – purity unspecified) was used to incorporate sodium in the glass matrix. The nominal composition of the glasses can be written as: $(100\text{-}x)(Ge_{25-y}Sb_{10}S_{65+y}) + x\text{Na}$ with x = 0, 2, 5.5 and y = 0, 2.5, 5, 7.5. Two series of compositions were selected. (1) The first one with varying S to Ge ratio (i.e., increasing amount of sulphur) and fixed sodium content: A-Na_2, B-Na_2, C-Na_2, D-Na_2 where x = 2 and y = 0, 2.5, 5, 7.5, respectively. (2) The second one, with varying sodium content and fixed S to Ge ratio: C-Na_0, C-Na_2, C-$Na_{5.5}$ where x = 0, 2, 5.5, and y = 5, respectively. These different parameters are summarized in the Table 1.

Table 1. The S/Ge ratio, the sodium content, the densities, and the glass transition temperatures of the synthetized glasses as well as the name they are referred to.

Sample	S/Ge ratio	Na content (at.%)	Density (g/cm^3)	T_g (°C)
A-Na_2	2.6	2	3.163 ± 0.006	313 ± 2
B-Na_2	3.0	2	3.099 ± 0.006	270 ± 2
C-Na_2	3.5	2	3.057 ± 0.012	241 ± 2
D-Na_2	4.1	2	2.982 ± 0.006	-
C-Na_0	3.5	0	3.06 ± 0.01	274 ± 2
C-$Na_{5.5}$	3.5	5.5	3.05 ± 0.01	250 ± 5

Raw materials for 15 g batches were weighed out in a glove box under nitrogen atmosphere and inserted in a quartz ampule. The system was put under vacuum (10^{-2} mbar) and sealed using an oxygen-methane torch. The sample was placed in a rocking furnace heated at a rate of 1 °C/min up to 850 °C for 12 h. After this time period, rocking was stopped, and the temperature decreased to 750 °C before quenching in water. The sample was then placed into an annealing furnace for 6 h at 40 °C below its glass transition temperature (T_g). Finally, glasses were cut and polished to obtain 1 mm thick disks of 1 cm diameter. The glass transition temperatures were determined by differential scanning calorimetry (Netzsch DSC 204 F1 Phoenix) using aluminum pans and a heating rate of 10 °C/min up to 550 °C. Glass densities were determined using the Archimedes method by immersing the samples in diethyl phthalate at room temperature. The measured T_g and densities are reported in the Table 1.

2.2 Vibrational spectroscopy

Raman spectroscopy to assess structural changes was carried out and two-dimensional spatial Raman intensity maps were acquired using a LabRAM HR Evolution (Horiba) spectrometer with a laser source at 785 nm and a 100× (N.A.= 0.9) objective with a one micron resolution.

2.3 Thermal poling

Thermal poling was performed under flowing nitrogen. The 1 cm diameter glass slides were heated up to 170 °C at a 15 °C/min rate (temperature fixed for all samples). A DC voltage of 3 kV was then applied (at a 320 V/min rate) by a 5 × 5 mm² electrode placed at the center of the glass disk and left on for 30 min. The samples were then brought back to room temperature before removal of the DC field. Two types of anodes were employed in this work. They consisted of a 100 nm platinum film deposited on a glass slide (5 × 5 × 1 mm^3) and were either (1) left as such (homogeneous electrodes that are everywhere conductive) or (2) lithographically structured to form (40 × 40 µm^2) non-conductive squared patterns delimited by 10 µm large conductive platinum grid. On the cathode side, a piece of silicon wafer was used, and a microscope coverslip was placed between the silicon and the sample to preserve the optical quality of the sample on this side.

2.4 Dissolution

Throughout this work, the solvent where the dissolution was carried out was EDA mixed at 15 volume % in dimethyl sulfoxide (DMSO). The dissolution of samples (i) prior to poling, (ii) after a homogenous poling, and (iii) after a structured poling were studied. For these three situations, different methods had to be developed to follow the dissolution rate. Specifically, (i) In order to track the dissolution rate of virgin glasses, we chose to look at the dissolved mass of the different samples with respect to the immersed time in the solvent. The one-centimeter square and 1 mm thick glass samples were weighted out with a 0.01 mg precision scale. They were immersed in the solvent and placed in an ultrasound bath for a given time. They were then rinsed with distilled water and dried before being weighted again and placed back to the ultrasound bath. (ii) To track the dissolution of the poled layer, weighting the samples is not adapted anymore as this layer is only several micrometer thick. Drawing on the methodology adopted by Reduto *et al.*, [23] we chose to protect a part of the surface with a metallic (gold) thin film (Q300TD, Quorum Technologies) and to measure the step height between the metallic film (not affected by the solvent) and the poled glass' surface with respect to the immersed time in the solvent. These measurements were also performed on virgin (non-poled) gold-protected samples for reference. The height step was measured with a Bruker's Dektak 6M stylus profiler. The measured height corresponded to the mean value of at least four measurements at each immersion time. Unlike the dissolution of the virgin glasses, the ultrasound bath was not used here to prevent the deterioration of the gold thin film. (iii) The samples poled with the structured electrode were immersed in the solvent in an ultrasound bath for different times. They were rinsed with distilled water, and dried. The topological profiles around the imprinted structures were then measured by atomic force microscopy (AFM) on an AFM Dimensions Icon Bruker instrument in PF-QNM mode. The topographic images were acquired using a ZYGO 6300 white-light interferometer.

3. Results

3.1 Dissolution of the virgin glasses

We first discuss the effect of the glasses' compositions on the dissolution rate of the samples prior to poling. In Fig. 1 are presented the dissolved masses with respect to the immersed time in the solvent. Fig. 1a illustrates the effect of varying sulphur content (for a fixed sodium content) while in Fig. 1b, the effect of the sodium content is investigated. On the first hand, from Fig. 1a, one can clearly observe that the higher the sulphur content is, the higher the dissolution rate is. The glass D-Na_2 is dissolved about four times faster than the stoichiometric glass (A-Na_2). On the other hand, the effect of the sodium content (Fig. 1b) is less pronounced. Taking into account the error bars, we can consider that, in the sodium concentration range evaluated in this study, the effect on the dissolution rate is negligible.

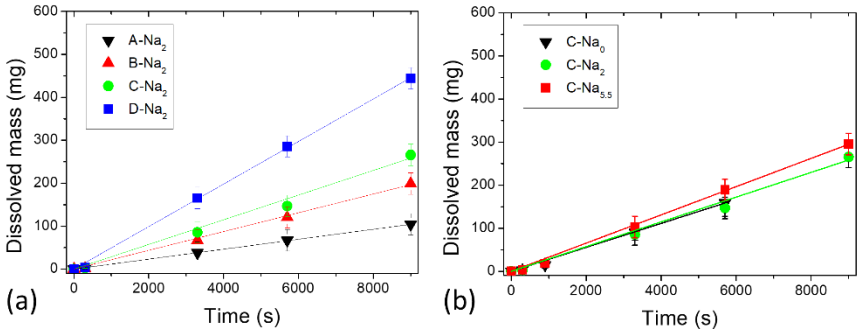

Fig. 1. Virgin glasses' dissolved mass with respect to time as a function of (a) the S/Ge ratio and of (b) the sodium content for 1 cm² area samples. The error was estimated to 25 mg to

account for the experimental error coming from the weighting and the sample's area estimation, the lines correspond to linear regressions.

3.2 Dissolution of homogenously poled glasses

To highlight the effect of poling and the resulting imparted change in the glass on the dissolution rate, the adopted methodology, as described in the experimental section, was to protect a part of the sample with a gold film and to measure the step height between this film and the glass as a function of the immersed time. Three compositions possessing two different S/Ge ratio and two different sodium contents – namely A-Na_2, C-Na_2 and C-$Na_{5.5}$ – were selected for evaluation. The results of this set of experiments are presented in Fig. 2. One can first notice a linear increase in the step height for the virgin glasses that enables the dissolution rate (v_{UP}) of virgin-like (unpoled) glass regions to be estimated. These values are gathered in the Table 2. From this table, it appears that C-$Na_{5.5}$ has the fastest dissolution rate, followed by C-Na_2 and A-Na_2. These observations are consistent with the dissolved mass evolutions seen in Fig. 1. In the poled samples, one can clearly identify two dissolution rates. First, the glass dissolves quicker than the virgin glass, and after a given time, the dissolution rate reaches that of the virgin glass. Here, the slope inflection point corresponds to the thickness of the poled layer, L_{poled}. For each sample, its value as well as the dissolution rate of the poled region (v_P) are reported in the Table 2.

In order to generate structures with a maximum contrast, it is crucial to consider Δh_{max}, the maximum gap between the poled and the unpoled zones. This parameter is illustrated by the schematic in Fig. 2d. It is formulated as Eq. (1):

$$\Delta h_{max} = L_{poled} - L_1 = L_{poled} - t_1 v_{UP} = L_{poled} - L_{poled}\frac{v_{UP}}{v_P} = L_{poled}\left(1 - \frac{v_{UP}}{v_P}\right) \quad (1)$$

From Eq.(1) and Fig. 2d, it follows that there are two methods to maximize Δh_{max}: having a sample exhibiting either a thick poled layer, or a large difference in dissolution rates of the poled and unpoled regions. In the selected compositions, two good candidates stand out: C-Na_2 with its eight microns-thick poled layer and C-$Na_{5.5}$ with a significant difference in dissolution rates of the poled and unpoled regions (lowest ratio v_{UP}/v_P, see Table 2).

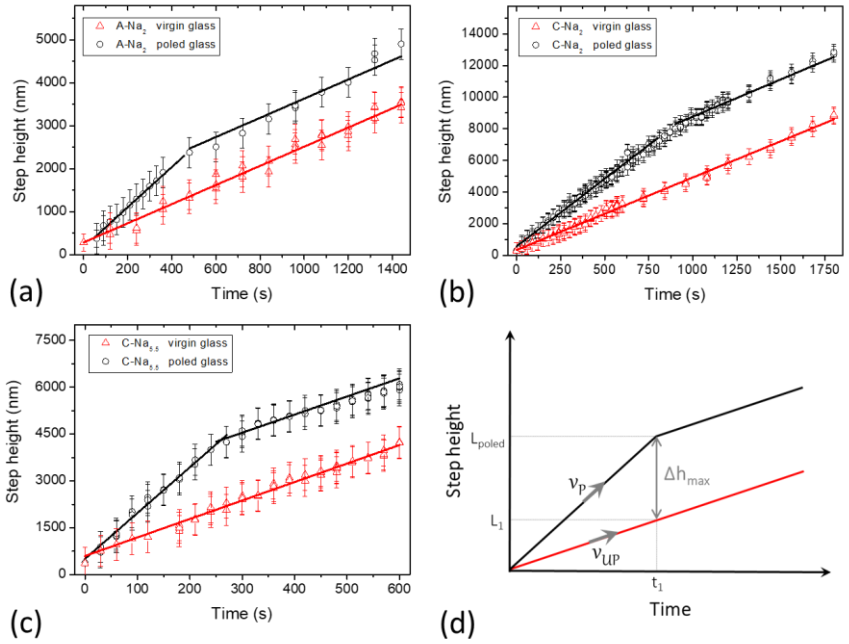

Fig. 2. Step heights measured between the protective gold film and the glass' surface as a function of the immersion time in the solvent for the compositions (a) A-Na_2, (b) C-Na_2, and (c) C-$Na_{5.5}$. The dots and lines correspond to the measured points and linear regressions, respectively. The error is mainly linked to the use of the profilometerand was estimated to be between 300 and 500 nm. The red lines and points correspond to the virgin glasses while the black ones correspond to the homogeneously poled samples. A schematic (d) illustrates the key parameters namely: L_{poled}, the poled layer thickness, v_P and v_{UP} the poled and unpoled dissolution speeds, and Δh_{max}, the maximum height that can be reached between the poled and the unpoled zones.

Table 2. Key parameters extracted from Fig. 2: poled zone's thickness, poled and unpoled regions' dissolution speeds, and their ratio as well as the theoretical maximal height that can be reached for each sample calculated from Eq. (1).

Sample	L_{poled} (µm)	v_P (nm/s)	v_{UP} (nm/s)	v_{UP} / v_P	Δh_{max} (µm)
A-Na_2	2.4 ± 0.3	4.7 ± 0.5	2.2 ± 0.2	0.47	1.3 ± 0.2
C-Na_2	8.0 ± 0.8	8.5 ± 0.9	4.7 ± 0.5	0.55	3.6 ± 0.4
C-$Na_{5.5}$	4.3 ± 0.4	14.7 ± 1.5	5.8 ± 0.6	0.39	2.6 ± 0.3

3.3 Dissolution of the micro-poled glasses

In this section, we no longer use a homogenous, two dimensional conductive electrode but an electrode that has been structured such that it allows for the micro-scale control of the poling process and opens the way for the design of surfaces for specific applications such as gratings. [22,24] As shown in prior work on this particular glassy system, the size and shape of the electrode influences the spatial extent of the electric field that serves to cause migration of the charged alkali ion (here sodium). [30,32] An optical image of the structured electrode used in this study is presented in Fig. 3a. It consists of a ten micron wide metallic grid separated by 40 × 40 µm² squares that are not conductive. Here, we define two regions on the micro-poled sample: the region in contact (IC) with the metallic grid during the process and the region not in contact (NIC) with the grid.

Following the methodology adopted in our previous works, [31,33] the effect of micro-poling (prior to any dissolution) on the glass' structure can be readily investigated by Raman microscopy. These results are presented for the C-$Na_{5.5}$ sample throughout Fig. 3. The Raman spectra extracted from the NIC and IC with the grid regions and are presented in the top part of Fig. 3b. Since only slight differences between these two spectra can be observed, the Raman difference spectrum (IC minus NIC) is also presented in Fig. 3b. The spatial evolution of the Raman response is illustrated by the cartographies of the five bands selected on the Raman difference spectrum.

In our previous work, a complete attribution of these bands is presented relying mainly on the works of Ward, [34] Lucovsky *et al.* [35] and Koudelka *et al.* [36] Specifically, in these glasses, antimony and sulphur form $SbS_{3/2}$ pyramids, while germanium is organized as $GeS_{4/2}$ tetrahedra. In glasses without sodium, the Sb-S stretching modes appear at 302 cm^{-1} [band (ii)]. When sodium is added, they shift to lower wavenumbers [band (i)]. The $GeS_{4/2}$ tetrahedra are mainly organized as corner sharing (CS) configuration [band (iii)] but also in edge sharing (ES) configuration [band (iv)]. Sodium-rich glasses present more ES units than sodium poor glasses, the opposite goes for CS units. As for the band (v), it is attributed to S-S homopolar bonds in S_n chains or S_8 rings.

In the present work, similar patterns are observed for all Raman intensity maps. In particular, sodium-rich glassy structures exhibit bands such as (i) and (iv) which are negative in the IC zones and positive in the NIC regions. The opposite behavior is seen for the sodium-poor glassy structures related bands such as bands (ii) and (iii). This conclusive variation in network configuration confirms the effectiveness of the micro-poling process that results in the micro-scale control of the structural variations as well as the observed sodium content distribution within that network.

The spatial intensity profile of the band (i) is shown in Fig. 3d. On this graph, the region between the dotted lines corresponds to the region IC defined by the metallic grid. As previously stated, this band is negative in this region but one can also notice a gradient in the intensity profile. The structural modifications are thus not only effective where the metallic electrode is in contact with the glass surface but they are also extend to adjacent regions to about five microns on each sides of the grid. In other words, there is not a perfect overlap between the IC and poled zones as well as between the NIC and unpoled regions: the poled zone extends beyond the IC zone. This is the result of an in-plane poling similar to that observed in other systems. [15,31,37,38] We have shown that it is possible to take advantage of this gradient in our previous work where we specifically aimed to design flat micro lenses through inducing a gradient in refractive index within this glassy system. [30]

Now that the microscale patterning of the structural variations generated by the micro-poling is confirmed, we now focus on the dissolution behavior of this sample. The topology profiles measured by AFM at different dissolution times are presented on the Fig. 3e. Immediately after poling (at t = 0 s), the sample's surface is flat. After immersion in the solvent, the IC zone can be seen to be selectively etched. This is consistent with the results from Fig. 2 where the poled samples exhibited more rapid dissolution than the virgin glasses. After 60 s of immersion, the glass surface forms a 1.7 µm high step; after 300 s, it reaches 3.7 µm. Comparing the AFM profiles with the Raman intensity profile from Fig. 3d, it appears that the shape of the etched structures reproduces exactly the structural modification gradient.

At longer dissolution times (at t = 1200 s), the structure's height reaches a plateau as shown in Fig. 4. This demonstrates that after this time, the whole poled layer thickness of the C-$Na_{5.5}$ sample was dissolved, and no further contrast between IC and NIC zones can be achieved. On this graph is also shown the maximal height measured by AFM as a function of the dissolution times for the two other selected samples, namely A-Na_2 and C-Na_2. It appears that for short

dissolution times (under 300 s), the generated structures are rather small (about 500 nm) for the A-Na_2 sample, bigger for C-Na_2 (2.1 µm), and the biggest for C-$Na_{5.5}$ (3.7 µm). If the later reached a plateau after 300 s, it is not the case of the other two samples. The step height continues increasing for C-Na_2 and A-Na_2, and respectively reaches 3.8 and 1.6 µm after 1200 s.

As predicted, in order to generate large topological contrasts, two parameters must be taken into account: (a) a significant difference in dissolution speeds of poled and unpoled regions and (b) a thick poled layer. From Fig. 3, it appears that the difference in dissolution speeds plays a major role during short dissolution times (C-$Na_{5.5}$ exhibits the biggest structures) while the thickness of the poled layer is a key parameter at longer dissolution times (C-Na_2 and C-$Na_{5.5}$ exhibit similar structure heights after 1200 s).

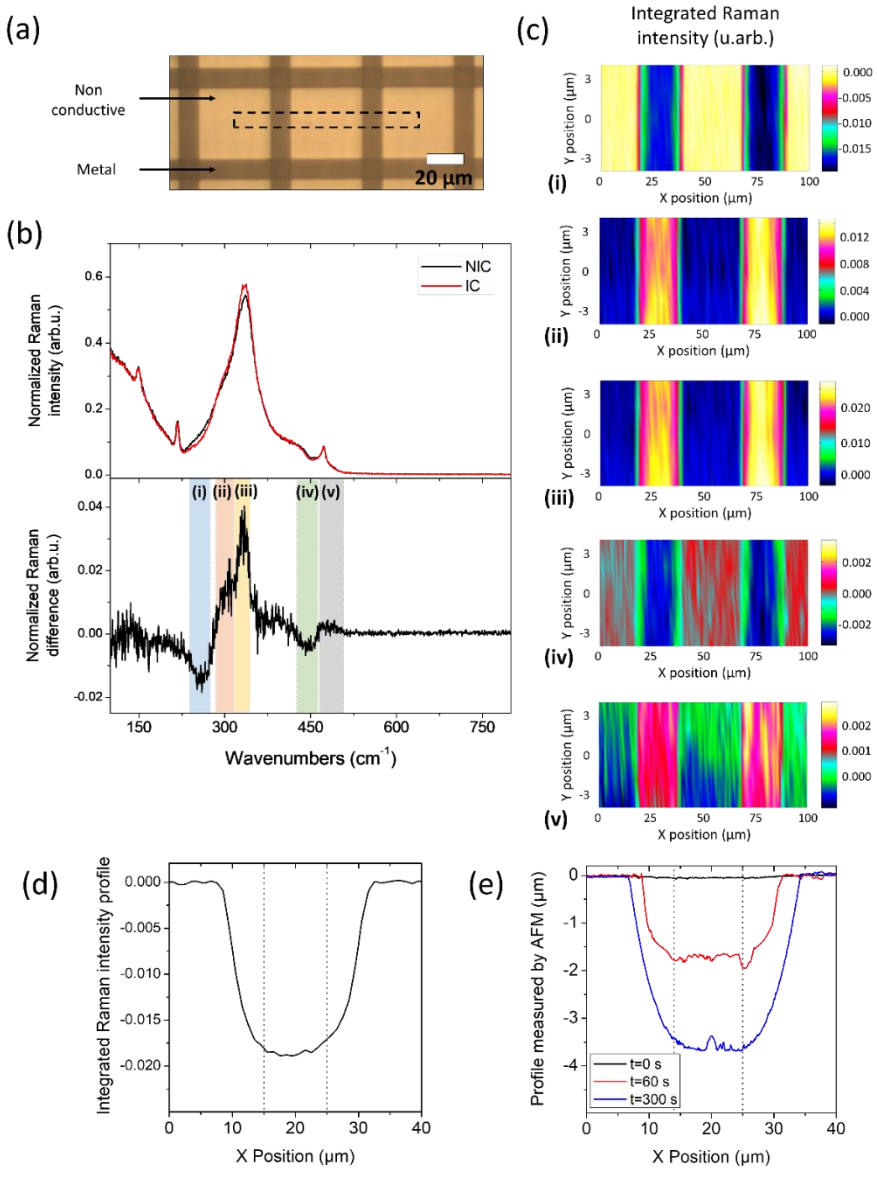

Fig. 3. (a) Optical image of the electrode employed for micro-poling with conductive and non-conductive zones highlighted. (b) Normalized Raman spectra extracted from the regions of the poled C-$Na_{5.5}$ glass that were in contact (IC) – in red – and non in contact (NIC) – in black – with the conductive zones of the electrode during the poling process and the Raman difference spectrum (spectrum IC minus NIC). (c) Spatial evolution of the selected bands from the Raman difference spectrum. (d) Intensity profile along the X position of the band (i)'s Raman intensity. (e) Topology of the sample measured by AFM in the same region upon dissolution for different times. The dotted lines in the two last graphs correspond to the metallic grid position during the poling treatment.

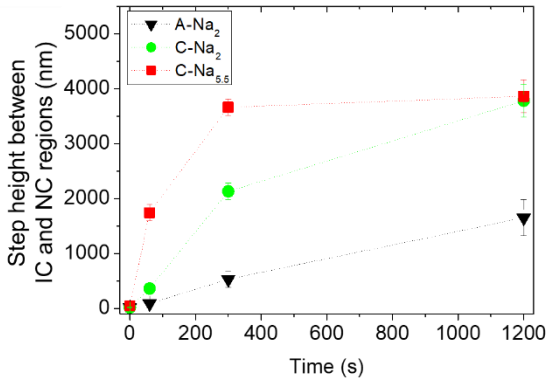

Fig. 4: Height of the step measured between the region in contact (IC) with the metallic part of the electrode during micro-poling and the one non in contact (NC) for the selected micro-poled samples as a function of the dissolution time. The dotted lines are guides for the eye, the experimental error is estimated to be of 10 %.

4. Discussion

Throughout the present work, we have demonstrated that in the glassy Ge-Sb-S-Na system, micro-poling followed by immersion in an amine solvent yields a structured topology of these glasses. A topological contrast as large as about four microns was obtained and is at least four times bigger than anything obtained by this process on silicate glasses. [22–25] Here we discuss the different parameters associated with the origin of this selective etching to shine the light on the different levers that one can have access to in order to control these structures.

Previous structural studies of this exact system [31,36] or related glassy systems [34,35] relying on Raman spectroscopy have shown that the higher the sulphur content, the more numerous the S-S homopolar bonds were. There are no S-S bonds in the stoichiometric glass (A-Na_2) since only one sulphur atom connects the different glass entities, forming $SbS_{3/2}$ pyramids and $GeS_{4/2}$ tetrahedra. [36] When sulphur is added, the interconnections between the different entities are made with more sulphur atoms. Sulphur atoms also form polymeric S_n chains as well as S_8 rings for high sulphur containing compositions.

As mentioned earlier, chalcogenide thin film synthesis via spin coating of dissolved glass solution has been the object of many studies with the objective of fabricating new planar photonic components. Dissolution mechanisms of these glasses in amine solvent were therefore at the center of interest of some of these studies. [39,40] They revealed that S-S homopolar bond are preferentially attacked by amine solvents, whereas heteropolar bonds are less reactive. These findings are also confirmed by studies focusing on sulfur-amine chemistry. [41] It follows then that the dissolution rate of glasses exhibiting a high S-S bonds content would be higher, consistent with what we observe with a slower dissolution rate of the stoichiometric glass (A-Na_2) as compared to that of the sulphur-rich glass (D-Na_2).

The comparison of the poled and virgin glasses' dissolution rates (Fig. 2) has revealed that in EDA, the poled zone was dissolved more rapidly than the unmodified one. One must note that this is not always the general behavior; for instance, acidic etching of poled silicate results in a faster dissolution rate of the unmodified region compared to the poled one. [22] In our previous work, the Raman study of these glasses (i) as a function of the sodium content and (ii) before and after poling has shown that the structural organization of a poled glass was similar to that of the glass without sodium. [31] In other words, the glass matrix was flexible enough to rearrange itself under the electric field and temperature combination to exhibit the composition and structure of a glass without sodium. However, the dissolution of virgin glasses with different sodium contents (Fig. 1b) has shown that the influence of the sodium content on the dissolution rate was negligible. Therefore, the poled region's selective etching cannot be explained by an effect of the structure nor composition.

A previous work on these glassy systems has demonstrated a control of the index variation by micro-poling. [30] A decrease in refractive index was observed in the poled regions (therefore, in the IC zones of the present work). Furthermore, on other glass systems, [33] we have demonstrated that this decrease in refractive index was linked to a decrease in the glass network's density upon poling. The higher the initial sodium content was, the larger the density decrease was. Recall, the difference in dissolution rates of poled and unmodified regions is larger for the sample C-$Na_{5.5}$ than for C-Na_2; that is, for a same S/Ge ratio, the difference is larger for higher initial sodium content. It follows that the selective etching of the poled region could be explained by this decrease in density that would facilitate the dissolution

One of the major advantages of this technique is illustrated in Fig. 5a: large areas can be structured at once. So far, only millimeter square surfaces were tested but as thermal poling can be readily scaled up to larger sizes in an efficient manner, it should also be extendable toward centimeter square areas. In Fig. 5b and Fig. 5c, one can see different kind of shapes that can be obtained by micro-poling and subsequent dissolution. This clearly demonstrates the versatility of this process with an accurate spatial control of the structures shapes that can be tuned easily by a control of the immersion time.

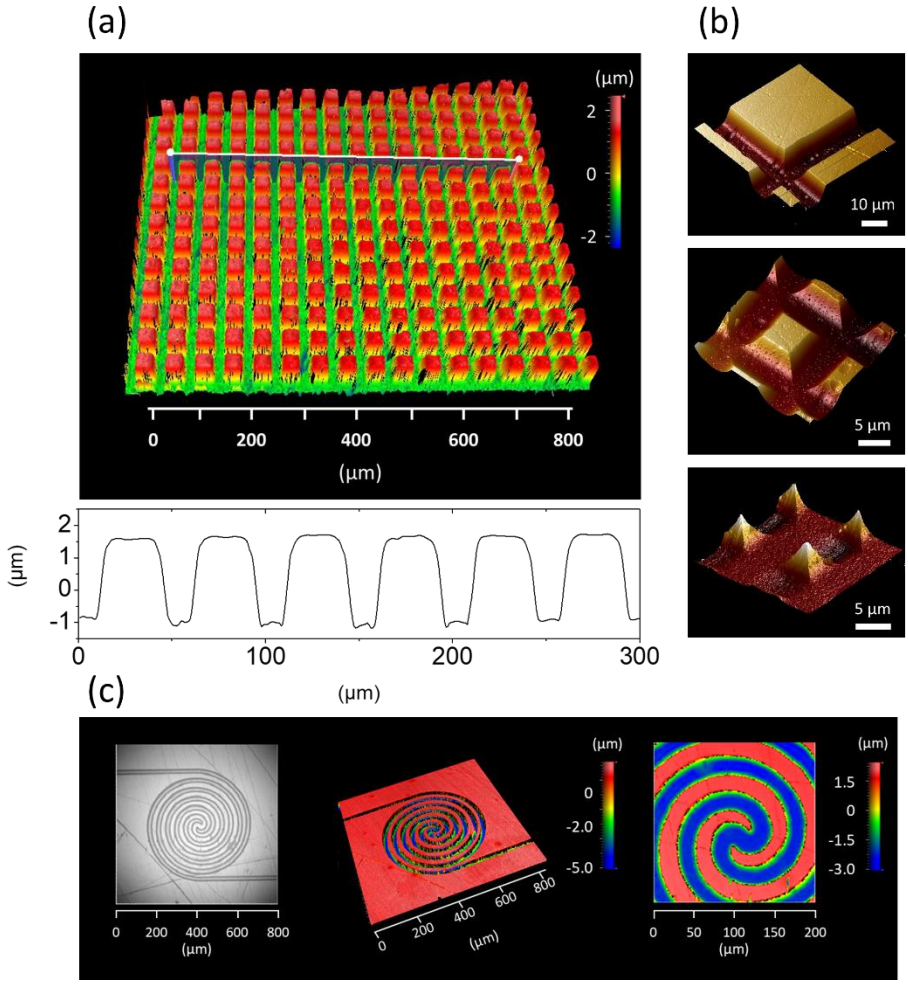

Fig. 5: (a) (top) Topography of a glass sample after micro-poling and dissolution measured by an optical profilometer giving evidence of the possibility to control the topology of large surfaces and (bottom) profile extracted from this image showing the regularity of the process. (b) AFM measured topographies of poled glasses at different dissolution times illustrating the different surface morphologies that can be obtained by this process. (c) Optical image (left) and topography (center and right) measured by an optical profilometer of a poled glass after dissolution. The structured electrode employed here consisted of lithographically made gold spiral. As opposed to previous patterns, here the conductive part is small (only the spiral). This kind of designs open possibilities in the domain of microfluidics for instance.

5. Conclusion

Throughout this work, we demonstrate a control of the topology of chalcogenide glasses by the combination of an electrothermal process and a chemical attack. The origin of the selective etching of the poled glasses was discussed: a decrease in the density upon poling is most likely at its origin. The influence of the composition (sulphur and sodium contents) was also evidenced. Significant (up to 4 µm) topological contrasts were achieved, and large (millimeter square) areas were structured. We have shown than a control of the spatial variations in size and shape (in 3-dimensions) was possible by tailoring the glass type, the electrode feature and the experimental conditions (of the poling and of the chemical attack). This process could be seen as an alternative to classical lithography techniques.

Funding

Idex Bordeaux (Cluster of Excellence LAPHIA), ANR-10-IDEX-03-02 and CNRS project EMERGENCE @INC2019. Horizon 2020 research program under the Marie Skłodowska-Curie grant agreement no. 823941 (FUNGLASS).

Acknowledgment

The authors gratefully acknowledge the financial support from IdEx Bordeaux (Cluster of Excellence LAPHIA and the allocated grant referred to as ANR-10-IDEX-03-03) and the CNRS project EMERGENCE @INC2019. This project has received funding from the European Union's Horizon 2020 research program under the Marie SkłodowskaCurie grant agreement no. 823941 (FUNGLASS). The authors would like to acknowledge the LAAS-CNRS Laboratory for the fabrication of the Pf-structured electrodes and the French RENATECH network. The Raman experiments were conducted using the SIV platform at the University of Bordeaux founded by the FEDER and the Region Aquitaine.

Disclosures

The authors declare no conflict of interest.

References

1. J. Nishii, K. Kintaka, and T. Nakazawa, "High-efficiency transmission gratings buried in a fused-SiO_2 glass plate," Appl. Opt. **43**, 1327 (2004).
2. T. Tamura, M. Umetani, K. Yamada, Y. Tanaka, K. Kintaka, H. Kasa, and J. Nishii, "Fabrication of Antireflective Subwavelength Structure on Spherical Glass Surface Using Imprinting Process," Appl. Phys. Express **3**, 112501 (2010).
3. Z. Han, P. Lin, V. Singh, L. Kimerling, J. Hu, K. Richardson, A. Agarwal, and D. T. H. Tan, "On-chip mid-infrared gas detection using chalcogenide glass waveguide," Applied Physics Letters **108**, 141106 (2016).
4. X. Cui, K. Tawa, H. Hori, and J. Nishii, "Duty ratio-dependent fluorescence enhancement through surface plasmon resonance in Ag-coated gratings," Appl. Phys. Lett. **95**, 133117 (2009).
5. G. Brière, P. Ni, S. Héron, S. Chenot, S. Vézian, V. Brändli, B. Damilano, J. Duboz, M. Iwanaga, and P. Genevet, "An Etching-Free Approach Toward Large-Scale Light-Emitting Metasurfaces," Adv. Optical Mater. **7**, 1801271 (2019).
6. H. Zuo, D.-Y. Choi, X. Gai, P. Ma, L. Xu, D. N. Neshev, B. Zhang, and B. Luther-Davies, "High-Efficiency All-Dielectric Metalenses for Mid-Infrared Imaging," Advanced Optical Materials **5**, 1700585 (2017).
7. M. Y. Shalaginov, S. An, Y. Zhang, F. Yang, P. Su, V. Liberman, J. B. Chou, C. M. Roberts, M. Kang, C. Rios, Q. Du, C. Fowler, A. Agarwal, K. A. Richardson, C. Rivero-Baleine, H. Zhang, J. Hu, and T. Gu, "Reconfigurable all-dielectric metalens with diffraction-limited performance," Nat Commun **12**, 1225 (2021).
8. Y. Zhang, C. Fowler, J. Liang, B. Azhar, M. Y. Shalaginov, S. Deckoff-Jones, S. An, J. B. Chou, C. M. Roberts, V. Liberman, M. Kang, C. Ríos, K. A. Richardson, C. Rivero-Baleine, T. Gu, H. Zhang, and J. Hu, "Electrically reconfigurable non-volatile metasurface using low-loss optical phase-change material," Nat. Nanotechnol. **16**, 661–666 (2021).
9. C. M. Schwarz, S. M. Kuebler, C. Rivero-Baleine, B. Triplett, M. Kang, Q. Altemose, C. Blanco, K. A. Richardson, Q. Du, S. Deckoff-Jones, J. Hu, Y. Zhang, Y. Pan, and C. Ríos, "Structurally and morphologically engineered chalcogenide materials for optical and photonic devices," J. Optical Microsystems **1**, (2021).
10. S. Y. Chou, "Nanoimprint lithography," J. Vac. Sci. Technol. B **14**, 4129 (1996).
11. T. Kohoutek, J. Orava, A. L. Greer, and H. Fudouzi, "Sub-micrometer soft lithography of a bulk chalcogenide glass," Opt. Express **21**, 9584 (2013).
12. H. Takagi, S. Miyazawa, M. Takahashi, and R. Maeda, "Electrostatic imprint process for glass," Applied physics express **1**, 024003 (2008).
13. N. Kubo, N. Ikutame, M. Takei, B. Weibai, S. Ikeda, K. Yamamoto, K. Uraji, T. Misawa, M. Fujioka, H. Kaiju, G. Zhao, and J. Nishii, "Nano-imprinting of surface relief gratings on soda-aluminosilicate and soda-lime silicate glasses," Opt. Mater. Express **7**, 1438 (2017).
14. P. N. Brunkov, V. G. Melekhin, V. V. Goncharov, A. A. Lipovskii, and M. I. Petrov, "Submicron-resolved relief formation in poled glasses and glass-metal nanocomposites," Tech. Phys. Lett. **34**, 1030–1033 (2008).
15. M. Dussauze, V. Rodriguez, F. Adamietz, G. Yang, F. Bondu, A. Lepicard, M. Chafer, T. Cardinal, and E. Fargin, "Accurate Second Harmonic Generation Microimprinting in Glassy Oxide Materials," Advanced Optical Materials **4**, 929–935 (2016).
16. A. A. Lipovskii, M. Kuittinen, P. Karvinen, K. Leinonen, V. G. Melehin, V. V. Zhurikhina, and Y. P. Svirko, "Electric field imprinting of sub-micron patterns in glass–metal nanocomposites," Nanotechnology **19**, 415304 (2008).
17. P. Brunkov, V. Goncharov, V. Melehin, A. Lipovskii, and M. Petrov, "Submicron surface relief formation using thermal poling of glasses," e-Journal of Surface Science and Nanotechnology **7**, 617–620 (2009).
18. N. Ikutame, K. Kawaguchi, H. Ikeda, D. Sakai, K. Harada, S. Funatsu, and J. Nishii, "Low-temperature fabrication of fine structures on glass using electrical nanoimprint and chemical etching," Journal of Applied Physics **114**, 083514 (2013).

19. D. E. Carlson, K. W. Hang, and G. F. Stockdale, "Ion Depletion of Glass at a Blocking Anode: II, Properties of Ion-Depleted Glasses," J American Ceramic Society **57**, 295–300 (1974).
20. W. Margulis and F. Laurell, "Interferometric study of poled glass under etching," Opt. Lett. **21**, 1786 (1996).
21. A. L. C. Triques, C. M. B. Cordeiro, V. Balestrieri, B. Lesche, W. Margulis, and I. C. S. Carvalho, "Depletion region in thermally poled fused silica," Appl. Phys. Lett. **76**, 2496–2498 (2000).
22. A. N. Kamenskii, I. V. Reduto, V. D. Petrikov, and A. A. Lipovskii, "Effective diffraction gratings via acidic etching of thermally poled glass," Optical Materials **62**, 250–254 (2016).
23. I. Reduto, A. Kamenskii, A. Redkov, and A. Lipovskii, "Mechanisms and Peculiarities of Electric Field Imprinting in Glasses," J. Electrochem. Soc. **164**, E385–E390 (2017).
24. I. Reduto, A. Kamenskii, P. Brunkov, V. Zhurikhina, Y. Svirko, and A. Lipovskii, "Relief micro- and nanostructures by the reactive ion and chemical etching of poled glasses," Opt. Mater. Express **9**, 3059 (2019).
25. S. E. Alexandrov, A. A. Lipovskii, A. A. Osipov, I. V. Reduto, and D. K. Tagantsev, "Plasma-etching of 2D-poled glasses: A route to dry lithography," Appl. Phys. Lett. **111**, 111604 (2017).
26. G. C. Chern and I. Lauks, "Spin-coated amorphous chalcogenide films," Journal of Applied Physics **53**, 6979–6982 (1982).
27. T. Kohoutek, T. Wagner, J. Orava, M. Krbal, A. Fejfar, T. Mates, S. O. Kasap, and M. Frumar, "Surface morphology of spin-coated As–S–Se chalcogenide thin films," Journal of Non-Crystalline Solids **353**, 1437–1440 (2007).
28. S. Song, N. Carlie, J. Boudies, L. Petit, K. Richardson, and C. B. Arnold, "Spin-coating of Ge23Sb7S70 chalcogenide glass thin films," Journal of Non-Crystalline Solids **355**, 2272–2278 (2009).
29. Y. Zou, H. Lin, O. Ogbuu, L. Li, S. Danto, S. Novak, J. Novak, J. D. Musgraves, K. Richardson, and J. Hu, "Effect of annealing conditions on the physio-chemical properties of spin-coated As_2Se_3 chalcogenide glass films," Opt. Mater. Express **2**, 1723 (2012).
30. A. Lepicard, F. Bondu, M. Kang, L. Sisken, A. Yadav, F. Adamietz, V. Rodriguez, K. Richardson, and M. Dussauze, "Long-lived monolithic micro-optics for multispectral GRIN applications," Sci Rep **8**, 7388 (2018).
31. R. Alvarado, L. Karam, R. Dahmani, A. Lepicard, F. Calzavara, A. Piarristeguy, A. Pradel, T. Cardinal, F. Adamietz, E. Fargin, M. Chazot, K. Richardson, L. Vellutini, and M. Dussauze, "Patterning of the Surface Electrical Potential on Chalcogenide Glasses by a Thermoelectrical Imprinting Process," J. Phys. Chem. C **124**, 23150–23157 (2020).
32. A. Lepicard, F. Adamietz, V. Rodriguez, K. Richardson, and M. Dussauze, "Demonstration of dimensional control and stabilization of second harmonic electro-optical response in chalcogenide glasses," Opt. Mater. Express **8**, 1613 (2018).
33. L. Karam, F. Adamietz, V. Rodriguez, F. Bondu, A. Lepicard, T. Cardinal, E. Fargin, K. Richardson, and M. Dussauze, "The effect of the sodium content on the structure and the optical properties of thermally poled sodium and niobium borophosphate glasses," Journal of Applied Physics **128**, 043106 (2020).
34. A. T. Ward, "Raman spectroscopy of sulfur, sulfur-selenium, and sulfur-arsenic mixtures," J. Phys. Chem. **72**, 4133–4139 (1968).
35. G. Lucovsky, F. L. Galeener, R. C. Keezer, R. H. Geils, and H. A. Six, "Structural interpretation of the infrared and Raman spectra of glasses in the alloy system Ge 1 − x S x," Phys. Rev. B **10**, 5134–5146 (1974).
36. L. Koudelka, M. Frumar, and M. Pisárčik, "Raman spectra of Ge□Sb□S system glasses in the S-rich region," Journal of Non-Crystalline Solids **41**, 171–178 (1980).
37. L. Karam, F. Adamietz, D. Michau, C. Gonçalves, M. Kang, R. Sharma, G. S. Murugan, T. Cardinal, E. Fargin, V. Rodriguez, K. A. Richardson, and M. Dussauze, "Electrically Micro-Polarized Amorphous Sodo-Niobate Film Competing with Crystalline Lithium Niobate Second-Order Optical Response," Advanced Optical Materials **8**, 2000202 (2020).
38. L. Karam, F. Adamietz, D. Michau, G. S. Murugan, T. Cardinal, E. Fargin, V. Rodriguez, K. A. Richardson, and M. Dussauze, "Second-Order Optical Response in Electrically Polarized Sodo-Niobate Amorphous Thin Films: Particularity of Multilayer Systems," Adv Photo Res 2000171 (2021).
39. S. Slang, K. Palka, L. Loghina, A. Kovalskiy, H. Jain, and M. Vlcek, "Mechanism of the dissolution of As–S chalcogenide glass in n-butylamine and its influence on the structure of spin coated layers," Journal of Non-Crystalline Solids **426**, 125–131 (2015).
40. Y. Zha, M. Waldmann, and C. B. Arnold, "A review on solution processing of chalcogenide glasses for optical components," Opt. Mater. Express **3**, 1259 (2013).
41. C. Wang, H. Chen, W. Dong, J. Ge, W. Lu, X. Wu, L. Guo, and L. Chen, "Sulfur–amine chemistry-based synthesis of multi-walled carbon nanotube–sulfur composites for high performance Li–S batteries," Chem. Commun. **50**, 1202–1204 (2014).